

## 2.5 Nanostructures and SI units

**Nanostructures** and their **quantisation effects** play a crucial role in recent definitions of the **electrical units**. To demonstrate the importance of precise definitions through fundamental constants, we will start with a brief history of units and measures.

For several millenia, people have been devising measures and artefacts for comparing unknown quantities with a known unit of measure. Historically, often body-related measures (thumb, ell, foot, step, span, ...) were chosen. In parallel, artefacts were prepared as rulers, or chiseled in stone as a universal measure for comparison. While indispensable for trade, architecture, science and many other areas, these units were prone to temporal changes, exhibited discrepancies between different specimen, were vulnerable to manipulation, and often changed locally from region to region. With increasingly exact measuring techniques and increasing globalization, it became more and more important to establish universal, ultra-high precision units with general validity. It was increasingly established that units can be mutually derived via the laws of physics, and that there exist natural constants which seem not to be changing with time, which could be determined with increasing precision as well.

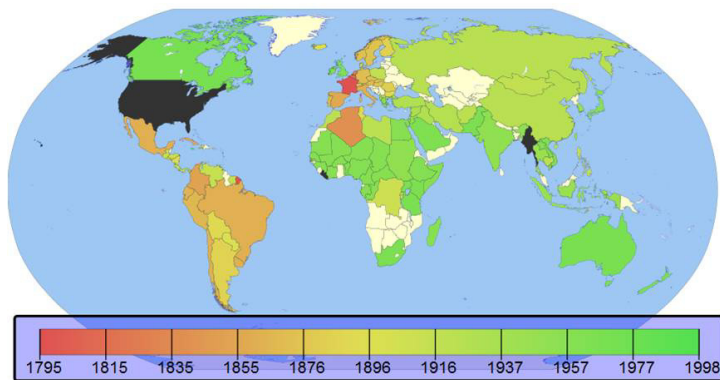


Fig. 2.63: Years in which the metric system was introduced in different countries across the world [commons.wikimedia.org/wiki/File:Metrication\_by\_year\_map.svg]

Starting with the French revolution, the **decimal system** was widely introduced across mainland Europe and South America. The spreading of the **metric system**, which uses the metre or its decimal multiples as a base unit, with time is visualized in Fig. 2.63.

Asia, Africa and Canada subsequently adopted the metric system over the course of the 20<sup>th</sup> century. The only countries not having officially adopted the metric system by now are Liberia, Myanmar, and the USA.

In 1799, **standards for 1 metre and 1 kilogram** were prepared from platinum and archived in Paris. These prototypes still exist, and while the metre had been redefined through the speed of light and the second by now, the kilogram was still being referred to an original prototype until the year 2019 while more precise and general definitions were being developed.

In 1874, the **CGS system** based on the units of **cm**, **g** and **s** was introduced under the influence of Gauss, Maxwell, and Thomson, followed by the introduction of

further practical units, such as the **Ohm, Volt and Ampère**. 1875 witnessed a milestone of the international implementation of the metric system in the signing of the **Metre Convention 1875** by 17 countries. The international office of weights and measures **BIPM (Bureau International de Poids es Mesures)** and the corresponding decision-making conference **CGPM (Conférence générale des poids et mesures)** were founded, which have been deciding about the introduction and redefinition of units ever since.

In 1889, new prototypes for the metre and kilogram were made, and the **MKS system** based on the m, kg and s was established.

1954 saw the introduction of new base units **Ampère, Kelvin and Candela**.

Recognizing the need for a consistent international system and definition of the units of measurement, in 1960 the BIPM introduced the **SI System (Système International d'Unités)** to facilitate the worldwide regulation and comparison of units of measures. The original base units were complemented by the unit **Mol** in 1971.

The SI system is now based on **7 base units plus many derived units**.

The 7 base units are: Metre (m), Kilogram (kg), Second (s), Ampère (A), Kelvin (K), Candela (cd), and Mol (mol).

The units and their interconnections are sketched in Fig. 2.64. They can be modified by prefixes (milli-, kilo-, nano-, etc.) and be combined to define derived units.

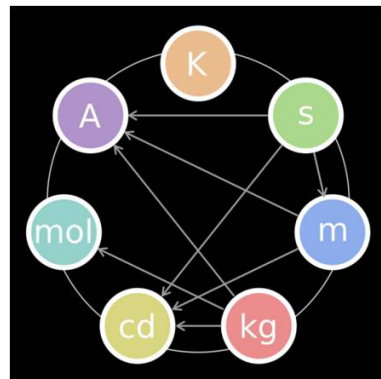


Fig. 2.64: The seven base units and their relations [<http://nagelhub.ning.com>]

Up until May 20<sup>th</sup> 2019, the seven base units were defined as follows:

- **Meter:** The meter was defined as the distance that light travels in vacuum within  $1 / 299.792.458$  s, where the speed of light  $c$  has been defined as a natural constant.
- **Kilogram:** The kilogram was still defined as the mass of the international prototype, a PtIr cylinder of 39 mm diameter, while alternative definitions based on natural constants were being developed.
- **Second:** The second was defined as 9.192.631.770 times the period of the radiation of the hyperfine transition of the ground state of  $^{133}\text{Cs}$  atoms.
- **Ampère:** The abstract definition of the Ampère was based on the strength of a constant electric current, which if flowing through two parallel, straight, infinitely

long conductors at a distance of 1 m in vacuum, would create a force of  $2 \cdot 10^{-7}$  N per meter between the wires.

- **Kelvin:** 1 K corresponded to  $1/273.16$  of the thermodynamic temperature at the triple point of water.
- **Mol:** 1 mol was the amount of matter of a particular system which consisted of the same number of individual particles as atoms are contained in 0.012 kg of  $^{12}\text{C}$ .
- **Candela:** 1 cd was the luminous intensity of a radiation source emitting monochromatic radiation of the frequency  $540 \cdot 10^{12}$  Hz, and the radiation power of which in a defined direction corresponds to 1/683 W/sr.

It is thus apparent that several of the units were based on physical prototypes that may change with time, or defined by abstract definitions that make comparison of measured data with the abstract unit difficult (especially for the Ampère). Therefore over the last decades, many efforts have been made towards **redefining the base units in terms of natural constants**. A suggestion of the links between the base units with corresponding natural constants is shown in Fig. 2.65.

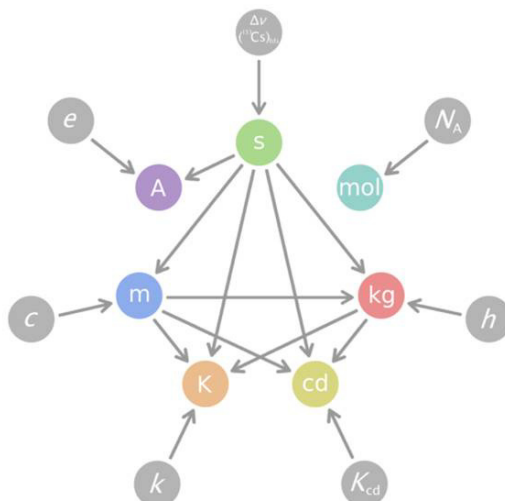


Fig. 2.65: Suggestions for linking the seven base units to fundamental constants

In 2011 it was resolved to attribute fixed, exact values to the fundamental constants  $h$  (**Planck's constant**),  $e$  (**elemental charge**),  $k_B$  (**Boltzmann constant**) and  $N_A$  (**Avogadro constant**), and to redefine the **kg**, **A**, **K** and **mol** by means of these constants. **s** and **m** were already defined through the value of  $c$  (**velocity of light**). The candela becomes a derived unit. For **A**, **K** and **mol**, the redefinition via  $e$ ,  $k_B$  and  $N_A$  was straightforward. Only the redefinition of the mass took longer, since the most advanced approaches of using a Watt balance ( $h$ ) or the crystal density of a sphere of single crystal silicon ( $N_A$ ) were only just reaching the required precision, such that all weights were still referred to the original PtIr prototype and its copies.

According to the redefinition of the base units, the relationships between the units for their respective calculation needed to be changing as well, as depicted in Fig. 2.66.

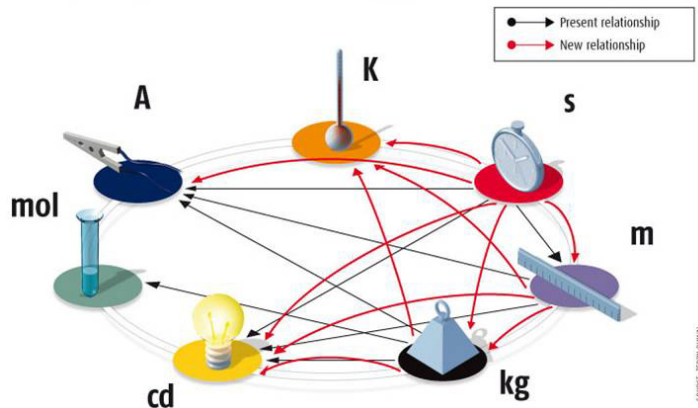


Fig. 2.66: New relationships between base units after redefinition via fundamental constants [www.newscientist.com]

For the **electrical units** Ampère and the derived units of Volt and Ohm, **nanostructures and their quantisation effects** as discussed over the course of this lecture course play a major role in linking the units to fundamental constants, and thus for their practical measurement by comparison to a known standard.

The units of voltage, current and frequency are connected via the **metrological triangle**, as shown in Fig. 2.67. For each leg of the triangle, two of the quantities are connected through a quantisation effect, which can be determined at ultra-high precision based on the natural constants **electrical charge  $e$**  and **Planck's constant  $h$** .

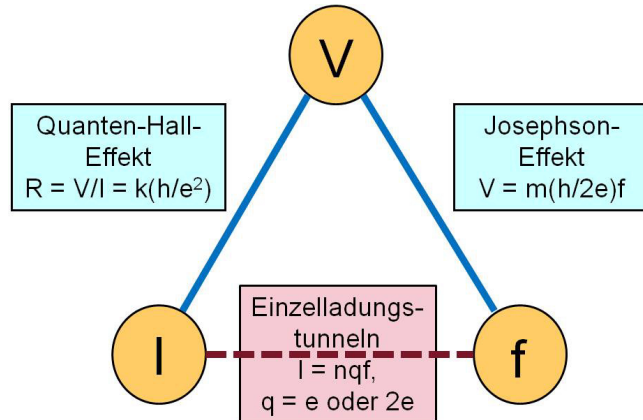


Fig. 2.67: The metrological triangle connecting voltage, current, and frequency [www.ptb.de]

The corresponding quantisation effects are discussed in this lecture course:

- **Quantum Hall effect:** The Hall resistance of a two-dimensional electron gas at low temperatures can be determined to extremely high precision from the plateaus occurring in the transversal resistance. The plateaus occur at values of  $R_H = h/(Ne^2)$  with  $N \in \mathbb{N}$ , which thus exclusively depend on the values of  $e$  and  $h$ . As a reminder, the longitudinal and the quantised transversal resistance are shown in Fig. 2.68. The quantities of  $I$  and  $V$  are connected through the value of  $R$ .

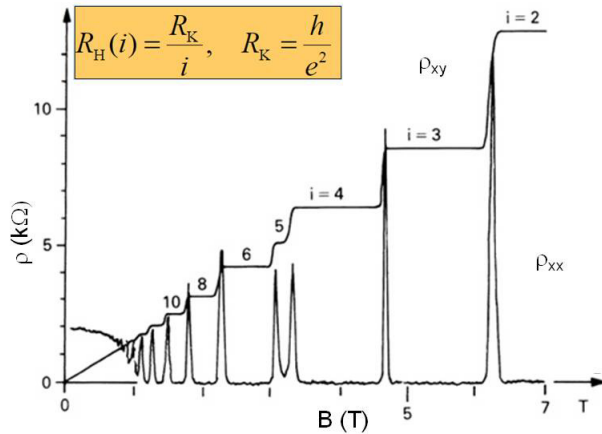


Fig. 2.68: Quantum Hall effect: quantized resistance in units of  $R_K = h/e^2$  [www.nonequilibrium.net]

- **Josephson effect:** The voltage across a normally conducting or isolating Josephson junction between two superconductors exhibits steps of  $U_J = Nfh/(2e)$ , with  $N \in \mathbb{N}$ , as shown in Fig. 2.69. The values thus exclusively depend on the values of  $e$  and  $h$ , and the high-precision microwave frequency  $f$ .

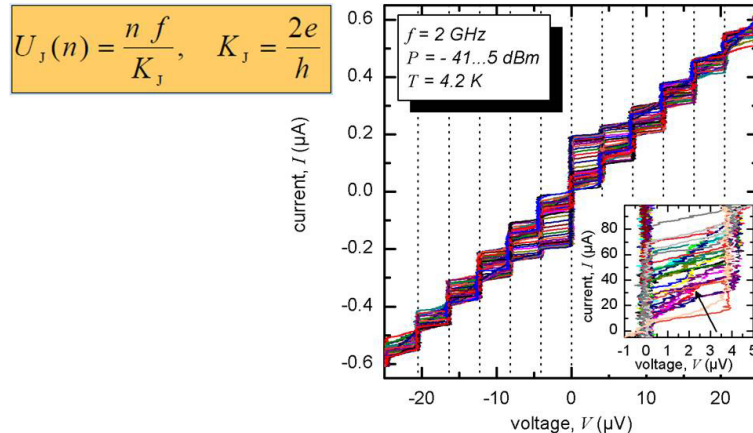


Fig. 2.69: Josephson effect: Quantized voltage in units of  $K_J = 2e/h$  [J. Pfeiffer et al., arXiv:0801.3229v1 (2008)]

- **Single electron tunneling:** As electrical current consists of discrete charge carriers moving with time, current can be measured in multiples of the charge  $e$  in single tunneling experiments through quantum dots. High-precision experiments are devised by fabricating so-called nano “turnstile”: Quantum dots for which the tunneling barriers to the left and right reservoirs are periodically increased and lowered by applying gate voltages with a microwave frequency  $f$ . For each cycle, a discrete number of electrons  $I = Nef$  with  $N \in \mathbb{N}$  can pass the quantum dot, leading to a highly precise standard for measuring  $I$ . An example of such a turnstile is shown in Fig. 2.70.

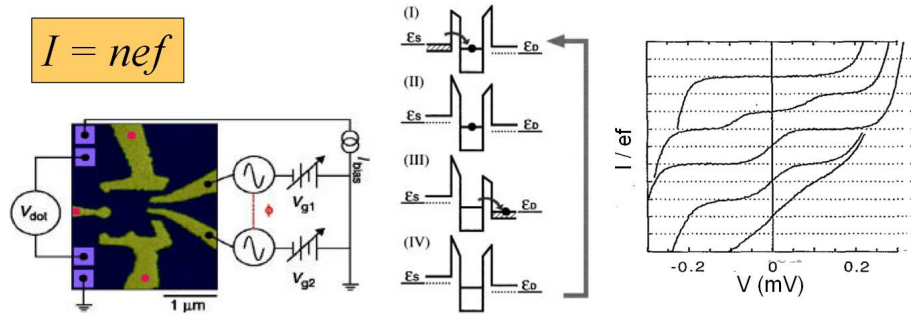


Fig. 2.70: Single electron tunneling: quantized current in units of  $e$ , (left) quantum dot with periodically driven gates, (center) schematic of the barrier-dependent single electron tunneling, (right) current quantized in units of  $ef$  [Y. Ono et al., Jpn. J. Appl. Phys. 42, L1109 (2003); www.visum-images.de; M. Switkes et al., Science 283, 1905 (1999); L.J. Geerlings et al., Phys. Rev. Lett. 64, 2691 (1990)]

The electrons are “counted”, which leads to an extremely precise standard to measure  $I$ . Record precisions down to less than  $2 \cdot 10^{-7}$  (PTB Braunschweig, 2.5.2017, <http://www.ptb.de>) have been achieved using this method, which were required to redefine the Ampère based on the elementary charge. A useful advance towards this purpose are “self referential” single electron pumps, which combine active electron transfer with in-situ detection (see L. Fricke et al., *Physik unserer Zeit* 2/2015 (46)). A corresponding circuit by the institute of metrology PTB is shown in Fig. 2.71.

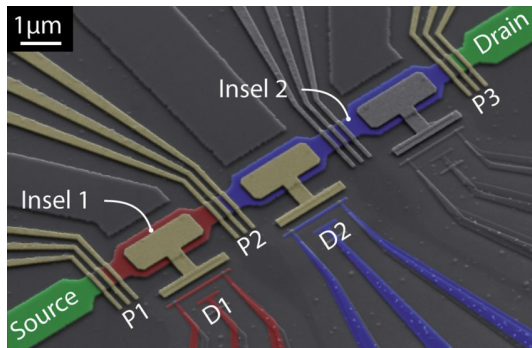


Fig. 2.71: Circuit to demonstrate the implementation of the Ampère based on  $e$ : Three single electron pumps P1 to P3 in series with capacitively coupled single electron detectors D1, D2 [L. Fricke et al., *Physik unserer Zeit* 2/2015 (46)]

Based on these immensely precise quantisation effects, which are fundamentally independent of the particular device in use and of the respective measurement setup, **new electric standards** were defined in 1990 for all practical purposes:

- The **voltage** was internationally defined through the Josephson effect, with the exact value of the **Josephson constant**  $K_J = \frac{2e}{h}$  defined as  $K_{J-90} = 483\,597.9 \text{ GHz/V}$ .
- The **resistance** was internationally defined through the quantum Hall effect, with the exact value of the **von Klitzing constant**  $R_K = \frac{h}{e^2}$  defined as  $R_{K-90} = 25\,812.807 \Omega$ .

Quantization effects in nanostructures are thus in constant use worldwide for each resistor that is being characterized and each voltage that is being measured.

With the redefinition of the current (i.e. the unit Ampère) based on the electronic charge in the year 2019 in the context of the general revision of the SI system in reference to natural constants, these definitions however became obsolete. Now the voltage and current can be derived from the constant definitions of e and h via the Josephson and quantum Hall effect.

### **Paradigm shift as of May 20<sup>th</sup> 2019: Redefinition of all SI units based on natural constants**

<https://www.bipm.org/fr/cgpm-2018/>,

<https://www.bipm.org/utils/common/pdf/CGPM-2018/26th-CGPM-Resolutions.pdf>

In recognition of the importance of an international system of units that is uniform and accessible world-wide, stable in the long term, internally self-consistent and practically realizable as well as based on the present theoretical description of nature at the highest level, the Bureau International des Poids et Mesures proposed a fundamental revision of the SI in 2011, to define the SI based on seven natural constants from which the definitions of the seven base units are deduced. At the 26<sup>th</sup> Conférence Générale de Poids et Mesures (CGPM) on November 16<sup>th</sup> 2018 in Versailles, groundbreaking resolutions with respect to the definitions of the SI system were adopted. It was decided that effective as of May 20<sup>th</sup> 2019, a new definition of the International System of Units, the SI system, was to be implemented. Rather than measuring the values of natural constants with increasing precision based on the fixed base units, the following natural constants are now defined as fixed values (without standard deviation):

- the unperturbed ground state hyperfine transition frequency of the caesium 133 atom  $\Delta\nu_{Cs} = 9\,192\,631\,770$  Hz,
- the speed of light in vacuum  $c = 299\,792\,458$  m/s,
- the Planck constant  $h = 6.626\,070\,15 \cdot 10^{-34}$  J s,
- the elementary charge  $e = 1.602\,176\,634 \cdot 10^{-19}$  C,
- the Boltzmann constant  $k = 1.380\,649 \cdot 10^{-23}$  J/K,
- the Avogadro constant  $N_A = 6.022\,140\,76 \cdot 10^{23}$  mol<sup>-1</sup>,
- the luminous efficacy of monochromatic radiation of frequency  $540 \cdot 10^{12}$  Hz  $K_{cd} = 683$  lm/W

where the hertz, joule, coulomb, lumen, and watt, with unit symbols Hz, J, C, lm, and W, respectively, are related to the units second, metre, kilogram, ampere, kelvin, mole, and candela, with unit symbols s, m, kg, A, K, mol, and cd, respectively, according to  $\text{Hz} = \text{s}^{-1}$ ,  $\text{J} = \text{kg m}^2 \text{s}^{-2}$ ,  $\text{C} = \text{A s}$ ,  $\text{lm} = \text{cd sr}$ , and  $\text{W} = \text{kg m}^2 \text{s}^{-3}$ .

All seven base units have been redefined with respect to these constants, see Fig. 2.72:

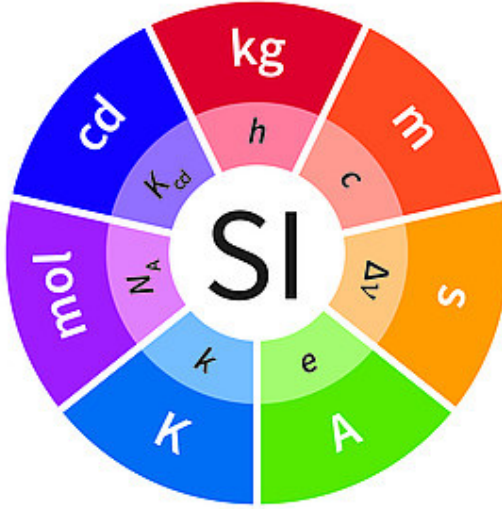


Fig. 2.72: Redefinition of the SI based on seven natural constants [<https://www.ptb.de/cms/forschung-entwicklung/forschung-zum-neuen-si/nachrichten/>]

- The **second**, symbol s, is the SI unit of time. It is defined by taking the fixed numerical value of the caesium frequency  $\Delta\nu_{Cs}$ , the unperturbed ground-state hyperfine transition frequency of the caesium 133 atom, to be 9 192 631 770 when expressed in the unit Hz, which is equal to  $s^{-1}$ .
- The **metre**, symbol m, is the SI unit of length. It is defined by taking the fixed numerical value of the speed of light in vacuum  $c$  to be 299 792 458 when expressed in the unit m/s, where the second is defined in terms of  $\Delta\nu_{Cs}$ .
- The **kilogram**, symbol kg, is the SI unit of mass. It is defined by taking the fixed numerical value of the Planck constant  $h$  to be  $6.626\ 070\ 15 \cdot 10^{-34}$  when expressed in the unit J s, which is equal to  $kg\ m^2\ s^{-1}$ , where the metre and the second are defined in terms of  $c$  and  $\Delta\nu_{Cs}$ .
- The **ampere**, symbol A, is the SI unit of electric current. It is defined by taking the fixed numerical value of the elementary charge  $e$  to be  $1.602\ 176\ 634 \cdot 10^{-19}$  when expressed in the unit C, which is equal to A s, where the second is defined in terms of  $\Delta\nu_{Cs}$ .
- The **kelvin**, symbol K, is the SI unit of thermodynamic temperature. It is defined by taking the fixed numerical value of the Boltzmann constant  $k$  to be  $1.380\ 649 \cdot 10^{-23}$  when expressed in the unit J K $^{-1}$ , which is equal to  $kg\ m^2\ s^{-2}\ K^{-1}$ , where the kilogram, metre and second are defined in terms of  $h$ ,  $c$  and  $\Delta\nu_{Cs}$ .
- The **mole**, symbol mol, is the SI unit of amount of substance. One mole contains exactly  $6.022\ 140\ 76 \cdot 10^{23}$  elementary entities. This number is the fixed numerical value of the Avogadro constant  $N_A$  when expressed in the unit mol $^{-1}$ , and is called the Avogadro number.
- The **candela**, symbol cd, is the SI unit of luminous intensity in a given direction. It is defined by taking the fixed numerical value of the luminous efficacy

of monochromatic radiation of frequency  $540 \cdot 10^{12}$  Hz,  $K_{cd}$ , to be 683 when expressed in the unit  $\text{lm W}^{-1}$ , which is equal to  $\text{cd sr W}^{-1}$ , or  $\text{cd sr kg}^{-1} \text{m}^{-2} \text{s}^3$ , where the kilogram, metre and second are defined in terms of  $h$ ,  $c$  and  $\Delta\nu_{Cs}$ .

The decision to adopt the conventional values of the Josephson constant  $K_{J-90}$  and of the von Klitzing constant  $R_{K-90}$  for the establishment of representations of the volt and the ohm using the Josephson and quantum Hall effects, respectively, was simultaneously abrogated.

These new definitions give precise, time-constant, practically realizable protocols that are no longer prone to artefacts, theft, temporal changes, drifts, etc. At the same time the redefinition means a fundamental paradigm shift in the way of thinking, fixing natural constants as an ever-constant, location-independent, variation-free reference frame rather than as physical entities to be explored by experiment. To keep the system self-consistent, at the same time the mass of the kilogram prototype, and the values of the vacuum magnetic permeability  $\mu_0 = 4\pi \cdot 10^{-7} \text{ H m}^{-1}$ , the thermodynamic temperature of the triple point of water  $T_{TPW} = 273.16 \text{ K}$  and the molar mass of carbon 12,  $M(^{12}\text{C}) = 0.012 \text{ kg mol}^{-1}$  that were taken as reference values before were changed from constants to experimental values. These were fixed to the above numbers with a relative standard uncertainty based on that of the corresponding natural constants at the time of the new definition. In future their values will be determined experimentally based on the new definitions.

The redefinition of the SI system will hardly be felt in everyday life, but has fundamental impact on the future of science and high-technology, and has brought the time-proven SI system up to speed with modern scientific development.

## 2.6 Carbon nanostructures

In nature, different **allotropes** of carbon exist. Allotropes are different structural modifications of an element, which in the case of carbon include structures of different dimensionalities, see Fig. 2.73. Several of these nanostructures have only been discovered over the last few decades. Carbon nanostructures thus offer a rich science kit for physical experimentation. The following structures are intensively researched:

- “3D / Bulk”: Diamond (tetrahedral) and graphite (stacks of two-dimensional sheets)
- “2D”: Graphene (single two-dimensional sheets)
- “1D”: Carbon nanotubes (rolled-up ribbons of graphene)
- “0D”: (Buckminster) fullerenes (spherical configurations,  $C_{60}$  or  $C_n$  with  $n \sim 20-200$ )

In the present case we focus on the properties of nanostructures and do not further discuss the 3D configurations.

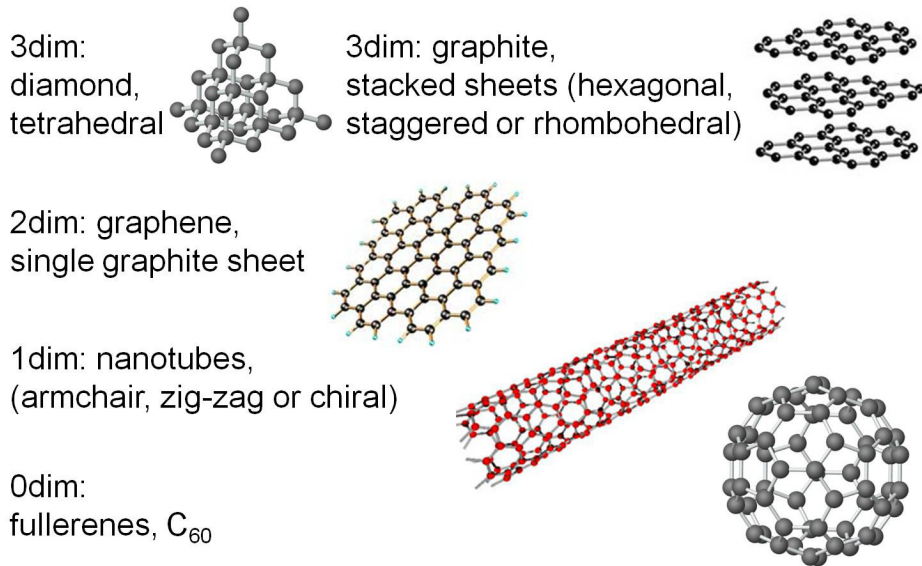


Fig. 2.73: Schematics of carbon allotropes with dimensionalities of 3D to 0D [cwx.prenhall.com, www.science.org.au, C. Ewels]

### 2.6.1 Graphene

Single sheets of graphene were first isolated and verified in 2004, which brought the Nobel prize to Andre Geim and Konstantin Novoselov in 2010.

Graphene consists in single atomic layers of ordered carbon atoms forming a honeycomb pattern with a thickness of few Ångstroms, as schematically shown in Fig. 2.74. It thus constitutes a stable true two-dimensional material. The honeycomb lattice is built from

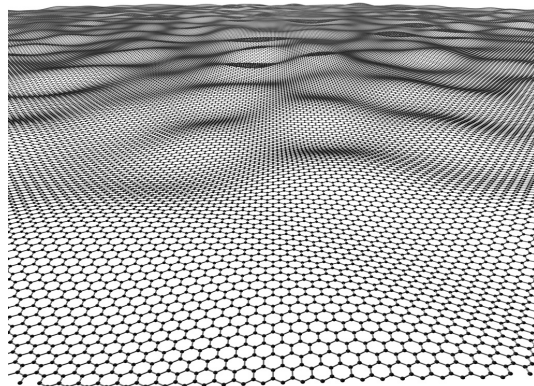


Fig. 2.74: Schematic of a wrinkled 2D graphene sheet with single atom thickness [<http://murdockcapital.com/wordpress2/2012/03/29/graphene/>]

two identical triangular sub-lattices that are shifted by one bond length of  $a_0 = 1.42 \text{ \AA}$ . The carbon atoms are connected via  $\sigma$ -bonds ( $\text{sp}^2$  hybridized), which are surrounded by a delocalized cloud of  $\pi$  electrons.

Due to its ultimate thinness and low optical absorption, imaging graphene is a challenging task. In optical and scanning electron microscopy, the contrast is very low, and in atomic force microscopy the topography is on the single nanometer scale. In transmission electron microscopy, the order of the carbon atoms is nicely visible. Figure 2.75 shows some examples of graphene imaged with different techniques.

General properties:

- High thermal conductance ( $\sim 5\,000 \text{ W m}^{-1} \text{ K}^{-1}$ )
- High mechanical stability, tensile strength  $\sim 1.25 \cdot 10^{11} \text{ Pa}$
- Large surface and high surface-to-volume ratio
- Light-weight, area density  $\sim 0.757 \text{ mg/m}^2$ :  $1 \text{ km}^2$  of graphene weighs only  $0.757 \text{ kg}$ !
- The graphene properties are strongly influenced by defects
- Defects: dislocations, edges, cracks, pentagons or heptagons, vacancies or adatoms
- High transparency: Only 2.3% of transmitted light are absorbed

## Electronic properties of graphene

Summary of the electronic properties:

- Excellent conductor with high electrical conductivity
- Universal conductance minimum of  $\sigma = \frac{4e^2}{h}$
- High mobilities ( $\sim 10^4 \frac{\text{cm}^2}{\text{Vs}}$ , record values of  $\sim 200.000 \frac{\text{cm}^2}{\text{Vs}}$ , long ballistic mean paths)
- The carrier type can be controlled via external gate voltages
- “Half-integer” quantum Hall effect
- The topology leads to quantum effects / Berry phase
- Experimental access to quantum mechanical & quantum electro-dynamic experiments

Graphene exhibits unique electronic properties. The band structure is depicted in Figure 2.76. Graphene is a zero band-gap semiconductor with  $E_g = 0$ , where the conductance band and the valence band only touch in single points in k-space (the Dirac points). Close to the Fermi energy, the two-dimensional system exhibits a linear

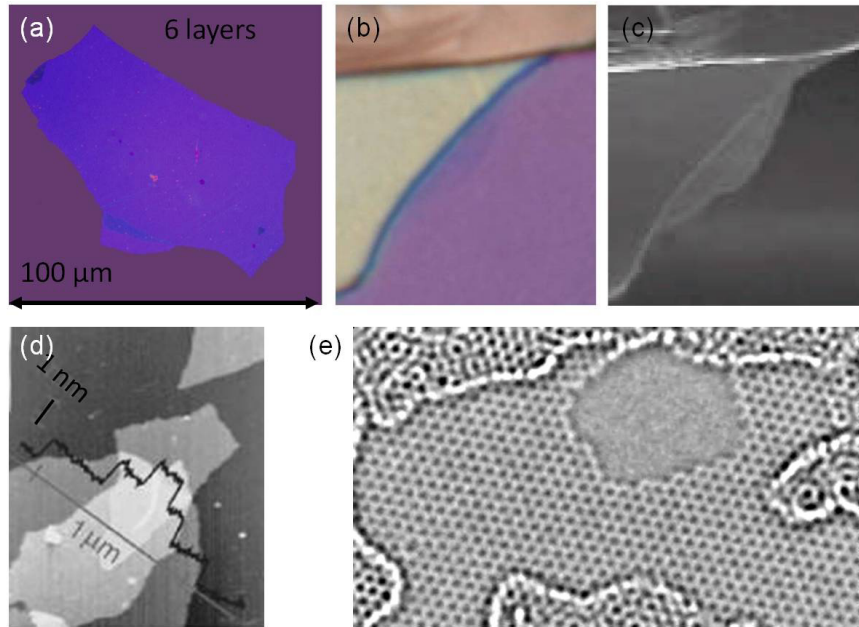


Fig. 2.75: Graphene imaged by (a,b) optical microscopy, (c) scanning electron microscopy, (d) atomic force microscopy, and (e) transmission electron microscopy [K. Novoselov et al., Science 306, 5696 (2004); S. Stankovich et al., Nature 442, 282 (2006); C.Ö. Girit et al., Science 323, 1705 (2009)]

dispersion relation. This fact strongly influences the charge carrier properties, which can be described within the formalism of mass-less Dirac fermions (“solid state quantum electrodynamics”). The charge carriers in graphene act like relativistic particles with an effective velocity  $v_F$ , where  $E(k) = \hbar v_F |\vec{k} - \vec{K}|$ , and the Fermi velocity (“effective speed of light”)  $v_F \simeq 10^6$  m/s.

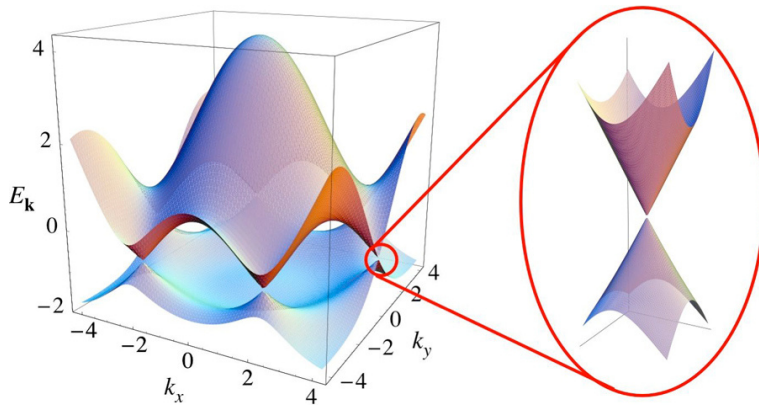


Fig. 2.76: Electronic dispersion of graphene. The conduction band and the valence band touch at six discrete points. These points are called  $K$  points or Dirac points. The six points can be divided into two inequivalent sets of three points each. The points within each set are all equivalent because they can be reached by reciprocal lattice vectors. The two inequivalent points are called  $K$  and  $K'$  and form the valley isospin degree of freedom in graphene. The zoom shows that the dispersion relation close to the  $K$  points looks like the energy spectrum of massless Dirac particles. [P. Recher and B. Trauzettel, Physics 4, 25 (2011)]

Calculating the dispersion relation of graphene based on the tight-binding-model

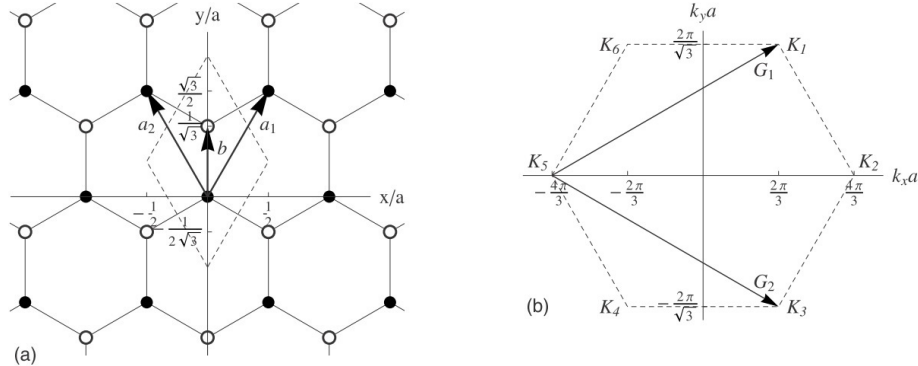


Fig. 2.77: (a) Schematic of the two Bravais sublattices (black vs. white circles) forming the honeycomb lattice of graphene, with the lattice vectors  $\vec{a}_1$  and  $\vec{a}_2$  indicated as given in the text, (b) Brillouin zone of graphene with the base vectors of the reciprocal lattice  $\vec{G}_1$  and  $\vec{G}_2$ . The vectors  $\vec{K}_i$  ( $i = 1..6$ ) correspond to the corners of the Brillouin zone, i.e. the Dirac points [T. Tudorovskiy and S. A. Mikhailov, Phys. Rev. B 82, 073411 (2010)]

The lattice vectors in the hexagonal lattice of graphene can be written as  $\vec{a}_1 = a(\frac{1}{2}, \frac{\sqrt{3}}{2})$ ,  $\vec{a}_2 = a(-\frac{1}{2}, \frac{\sqrt{3}}{2})$ , with the magnitude of the vector  $a = |\vec{a}_1| = |\vec{a}_2| = \sqrt{3}a_0$ , see Fig. 2.77, and the spacing between neighbouring carbon atoms  $a_0 = 1.42 \text{ \AA}$ .

The Ansatz for the wave function in this system can be written as  $\psi_{\vec{k}} = \sum_{\vec{R} \in G} e^{i\vec{k}\vec{R}} \phi(\vec{x} - \vec{R})$ , with the lattice vector space  $G$ .

$\phi(\vec{x})$  are the atomic wave functions of the  $sp_z$ -orbitals perpendicular to the plane of the graphene. Each unit cell contains two  $p_z$ -orbitals  $\phi_1$  and  $\phi_2$ , which are assumed to be localized at the positions  $\vec{x}_1$  and  $\vec{x}_2$  of the corresponding C atoms in the unit cell. The complete wave function is a linear combination  $\phi(\vec{x}) = b_1\phi_1(\vec{x}) + b_2\phi_2(\vec{x}) = \sum_n b_n\phi_n$ .

In the following, the Hamilton operator for a single electron in the potential of the C atoms at the positions  $\vec{x}_1, \vec{x}_2$  can be formulated:

$$H = \frac{\vec{p}^2}{2m} + \sum_{\vec{R} \in G} \left( V_{at}(\vec{x} - \vec{x}_1 - \vec{R}) + V_{at}(\vec{x} - \vec{x}_2 - \vec{R}) \right)$$

Applying the Hamilton operator to  $\phi_1$  and  $\phi_2$ , the following two equations ensue:  $H\phi_{1,2} = \epsilon_{1,2} + \Delta U_{1,2}\phi_{1,2}$ .

Here  $\epsilon_1 = \epsilon_2$  is the eigen value of the  $p_z$  states, and

$$\Delta U_1 = \sum_{\vec{R} \neq 0} \left( V_{at}(\vec{x} - \vec{x}_1 - \vec{R}) + V_{at}(\vec{x} - \vec{x}_2 - \vec{R}) + V_{at}(\vec{x} - \vec{x}_2) \right), \Delta U_2 \text{ analogous.}$$

The zero-point for the energy can be freely chosen:

be  $\epsilon_{1,2} = 0 \Rightarrow H\phi_1 = \Delta U_1\phi_1$  and  $H\phi_2 = \Delta U_2\phi_2$ .

Note that  $\Delta U_{1,2}\phi_{1,2}$  is small, since  $\Delta U$  is negligible close to the atom, and  $\phi$  vanishes far away from the atom.

The Schrödinger equation  $H\psi_{\vec{k}} = E(\vec{k})\psi_{\vec{k}}$  can be solved by projecting  $\psi$  onto the two states  $\phi_1$  and  $\phi_2$ :

$$E(\vec{k}) \langle \phi_j | \psi \rangle = \langle \phi_j | \Delta U_j | \psi \rangle \quad (2.84)$$

The corresponding terms can now be calculated under the assumption that only the overlap integrals up to the order of next neighbours need to be taken into account.

$$\text{Be } \gamma_0 = \int \phi_1^* \phi_2 = \int \phi_2^* \phi_1 \in \mathbb{R} \text{ and } \gamma_1 = \int \phi_1^* \Delta U_1 \phi_2 = \int \phi_2^* \Delta U_2 \phi_1.$$

The following four equations are obtained:

$$\langle \phi_1 | \psi \rangle = b_1 + b_2 \gamma_0 (1 + e^{-i\vec{k} \cdot \vec{a}_1} + e^{-i\vec{k} \cdot \vec{a}_2}) \quad (2.85)$$

$$\langle \phi_2 | \psi \rangle = b_2 + b_1 \gamma_0 (1 + e^{i\vec{k} \cdot \vec{a}_1} + e^{i\vec{k} \cdot \vec{a}_2}) \quad (2.86)$$

$$\langle \phi_1 | \Delta U_1 | \psi \rangle = b_2 \gamma_1 (1 + e^{-i\vec{k} \cdot \vec{a}_1} + e^{-i\vec{k} \cdot \vec{a}_2}) \quad (2.87)$$

$$\langle \phi_2 | \Delta U_2 | \psi \rangle = b_1 \gamma_1 (1 + e^{i\vec{k} \cdot \vec{a}_1} + e^{i\vec{k} \cdot \vec{a}_2}) \quad (2.88)$$

where the abbreviation  $\alpha(\vec{k}) = (1 + e^{-i\vec{k} \cdot \vec{a}_1} + e^{-i\vec{k} \cdot \vec{a}_2})$  ( $\alpha^*(\vec{k})$  analogous) can be introduced.

From the resulting eigenwert problem, the dispersion relation is determined by setting the determinant to zero and approximating  $\gamma_0 \simeq 0$ , resulting in:

$$E(\vec{k}) = \pm \gamma_1 \sqrt{1 + 4 \cos\left(\frac{a}{2} k_x\right) \cos\left(\frac{\sqrt{3}a}{2} k_y\right) + 4 \cos^2\left(\frac{k_x a}{2}\right)} \quad (2.89)$$

From the above results, the linear dispersion of graphene close to the Fermi energy can be shown as well as that fact that the bands touch in the Dirac points, i.e.  $E(\vec{K}_i) = 0$ .

By introducing doping / impurities, the band gap can be opened to lead to an increasingly semiconductor-like behaviour.

By applying either positive or negative gate voltages through gating, the chemical potential can be shifted into either the conductance or the valence band as shown in Fig. 2.78. This leads to the accumulation of either electrons in the conductance band, or holes in the valence band. Depending on the polarity of the external gate voltage, graphene becomes either n- or p-conducting. This behaviour is called **ambipolar**. In defect-free graphene no scattering centers exist, thus theoretically very high carrier mobilities could be reached. A main difficulty for real-life devices consists in the presence of edges, through which scattering is introduced.

The conductivity of graphene exhibits a universal minimum value, the quantum unit of conductivity, which is intrinsic to Dirac systems and can be determined to  $\sigma_{min} = (4e^2)/h$ . Accordingly, the maximum resistivity is always measured to be  $\rho_{max} = h/(4e^2)$ , independent of the particular device geometry or carrier mobility. A gate-dependent measurement of the conductivity showing the finite minimum, and a comparison of  $\rho_{max}$  for different mobilities are shown in Fig. 2.79.

The quantisation observed in the quantum Hall effect for graphene differs from the one discussed for other 2dim systems before, which showed 2-fold degenerate quantisations in steps of  $(2e^2)/h$ . As shown in Fig. 2.80, the Shubnikov-de Haas-oscillations in the longitudinal resistivity display one single continuous set of oscillations for both electrons and holes ( $n < 0$  and  $n > 0$ ). The oscillations exhibit a constant frequency in  $B$  and are 4-fold degenerate (2-fold spin degeneracy plus 2-fold valley degeneracy). The Hall conductivity is quantised in a sequence of  $(4e^2/h)$  ( $N + 1/2$ ) with a step-height of  $\Delta\sigma_{xy}$

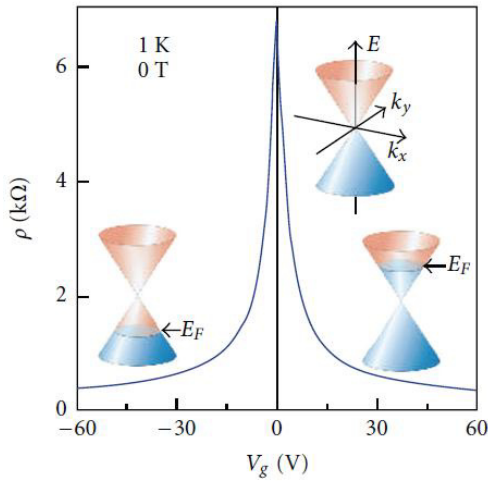


Fig. 2.78: Ambipolar electric field effect in graphene; the insets show the changes in the position of the Fermi level  $E_F$  as a function of gate voltage [D. Cooper et al., ISRN Condensed Matter Physics, Article ID 50168625 (2012), doi:10.5402/2012/501686]

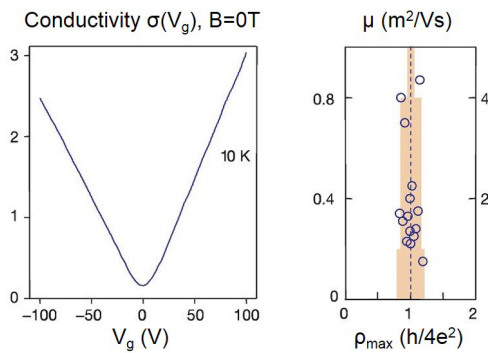


Fig. 2.79: Left: conductivity  $\sigma(V_g)$  displaying a minimum; right: quantized unit of conductivity, visible in  $\mu(\rho_{max})$  [K. Novoselov et al., Nature 438, 197 (2005)]

$= (4e^2)/h$  for all steps, including the transition from the lowest hole Landau level to the lowest electron Landau level. All Landau levels are 4-fold degenerate. At  $E = 0$  only one projection of the pseudospin is accommodated, while the level is shared by electrons and holes. The situation already changes dramatically for two-layer graphene, as shown in the inset of Fig. 2.80. Here  $\Delta\sigma_{xy} = (4e^2)/h$  remains valid for both electrons and holes, but the sequence changes to  $(4e^2/h) N$ , with a gap of  $(8e^2)/h$  around  $n = 0$ .

### Preparation and structuring:

Novel procedures for producing defect-free single-layer graphene over large areas are intensely researched as a key enabler for future graphene technologies. So far, e.g. the following procedures are commonly used for synthesizing graphene:

- Mechanical exfoliation of highly oriented pyrolytic graphite (HOPG): Historically first method, repeated “scotch-tape” peeling and transfer of graphite flakes from a

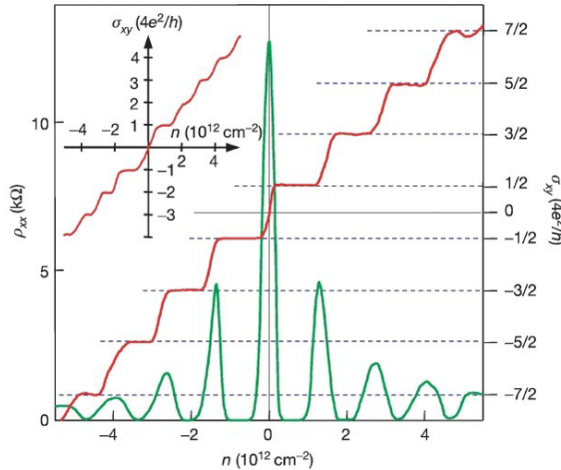


Fig. 2.80: Quantum Hall effect for massless Dirac fermions in single-layer graphene ( $B = 14$  T,  $T = 4$  K), quantised in half-integer multiples of  $(4e^2)/h$ . The inset shows the quantum Hall effect for two-layer graphene, which is quantised in integer multiples of  $(4e^2)/h$  [K. Novoselov et al., Nature 438, 197 (2005)]

three-dimensional stack of graphite until few or single layers of graphene are obtained; identification by optical microscopy.

- Thermal decomposition of silicon carbide (SiC): At high temperatures (1000–1500 °C) in UHV Si is sublimated from the surface, and a top layer of carbon forms on the SiC substrate.
- Chemical vapour deposition (CVD): A single crystal catalyst layer (e.g. Cu, Ni) is heated to several hundred degrees, and carbon-containing gases are decomposed at the surface by the catalyst, forming single-layer graphene under suitable conditions.
- Other approaches: Molecular beam epitaxy; sodium-ethanol pyrolysis; reduction of graphene oxide; slicing carbon nanotubes to create graphene nano-ribbons; liquid precursor deposition

From the original micro-flakes of graphene, today's processes could already be scaled up to almost square meters, see Fig. 2.81. Graphene can be structured using the micro- and nanofabrication techniques described in the previous chapters. In particular, graphene sheets can be transferred from one substrate to another by etching away the first substrate, or making use of different surface energies. The graphene can be covered by a resist layer, and optical or electron beam lithography can be performed to protect only the envisaged graphene structure by resist. The surrounding graphene layer may be etched away e.g. by oxygen plasma. After removing the resist, a conducting graphene structure suitable for electronic measurements is shaped and can be contacted by metal pads. One such example of a graphene Hall bar is shown in Fig. 2.82.

Method	Layers	Size	Mobility ( $\text{cm}^2\text{V}^{-1}\text{s}^{-1}$ )
Exfoliation	1 to 10+	1 mm <sup>a</sup>	15000 <sup>b</sup>
Thermal SiC	1 to 4	50 $\mu\text{m}$ <sup>c</sup>	2000 <sup>c</sup>
Ni-CVD	1 to 4	1 cm <sup>d</sup>	3700 <sup>d</sup>
Cu-CVD	1	65 cm <sup>e</sup>	16000 <sup>f</sup>

Fig. 2.81: Graphene properties achieved with different fabrication techniques [D.R. Cooper et al., Con. Matt. Phys. 2012, 7 (2012)]

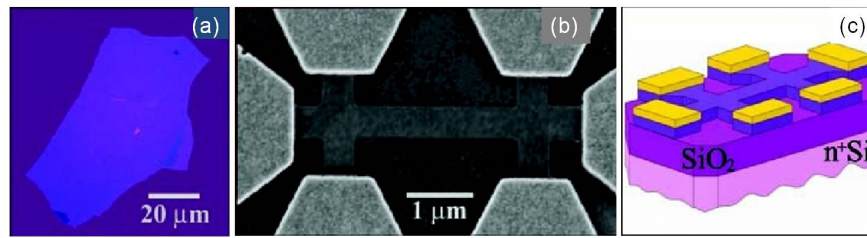


Fig. 2.82: (a) Optical image and (b) contacted Hall-bar fabricated from a graphene flake, (c) schematic of the graphene device [Novoselov et al., Science 306, 666 (2004)]

### Device applications:

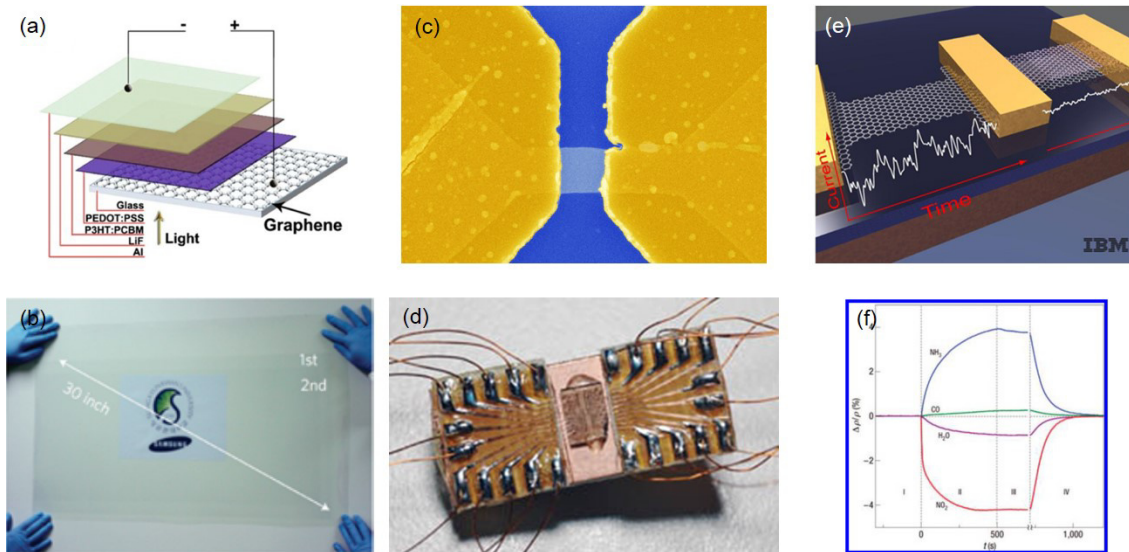


Fig. 2.83: (a) Schematics of an organic solar cell with a transparent graphene electrode; (b) display from multiple CVD-grown graphene sheets transferred to PET; (c) single-layer graphene transistor; (d) proof-of-principle all-graphene circuitry device; (e) schematic of a graphene gas sensor; (f) sensor signal  $\Delta\rho/\rho(t)$  of NH<sub>3</sub>, CO, H<sub>2</sub>O, and NO<sub>2</sub> molecules [D.R. Cooper et al., Cond. Matt. Phys. 2012, 9 (2012); Science 306, 5696 (2004); Giorgia Tech Research News 4/2006; M.J. Allen et al., Chem. Rev. 110, 132 (2010)]

Graphene has created enormous interest as a future device material due to its small weight, thinness, high transparency, excellent conductivity, mechanical strength, and

unique optical and electronic properties. First demonstrated devices include transistors, screens, or highly sensitive chemical sensors. Graphene may be imagined as transparent conducting electrodes for displays, touch screens, or photovoltaic cells. Compared to the commonly used indium tin oxide (ITO), which exhibits a sheet resistance of  $\sim 100 \Omega/\square$  and a transmission of  $\sim 90\%$ , single layer graphene surpasses these properties with a sheet resistance of  $\sim 30 - 100 \Omega/\square$  and a transmission of up to  $\sim 97.7\%$ . Graphene ribbons have been introduced as the conducting channel in field-effect transistors on  $\text{SiO}_2/\text{Si}$  with metal contacts, providing fast switching times through high charge carrier mobilities. In 2006 a first all-graphene circuitry planar field-effect transistor was demonstrated. Due to their ultra-high surface-to-volume-ratio, graphene layers can be applied as high-sensitivity sensors. The ambipolar behaviour leads to “chemical gating” when molecules from the gas phase are adsorbed on the graphene. The resistivity change of the graphene ribbon due to a change in the local potential is measured, and the original resistivity is recovered when the adsorbate is removed. The sensitivity offers the potential of single molecule detection. Examples of proof-of-principle devices are depicted in Fig. 2.83. Large sums of research and development funding are currently directed towards further developing graphene technology. However several practical issues will need to be solved before graphene becomes a serious competitor to current standard materials.

### Other two-dimensional layer structures:

Researchers recently attempted to mimick graphene by artificially ordering different building blocks in honeycomb lattice geometries comparable to the carbon atoms in graphene. Such artificial honeycomb lattices offer tunable platforms for studying massless Dirac quasi-particles [cf. M. Polini et al., *Nature Nanotechnology* 8, 625 (2013)]. As building blocks, nano-patterned two-dimensional electron gases, molecule-by-molecule assembly (e.g. of CO) by scanning probe manipulation, or optical trapping of ultracold atoms were pursued. By these methods, some of the characteristic properties of graphene could actually be reproduced.

Other two-dimensional systems that are currently under intense investigation are the so-called **transition metal dichalcogenides (TMDs)**, compounds with a chemical structure of  $\text{MX}_2$ , where M represents a transition metal and X is the chalcogen such as S, Se or Te. So far about 40 different layered TMD compounds are known, including insulators, semiconductors, semimetals and metals. Recent studies focus on semiconducting two-dimensional crystals, with prominent examples such as  $\text{MoS}_2$ ,  $\text{MoSe}_2$ ,  $\text{WSe}_2$  or  $\text{WS}_2$ . These exhibit unusual electronic and optical properties: for example, single layers of the TMDs exhibit direct band gaps, making them attractive for optical applications, whereas their bulk counterparts (starting already from double layers) represent indirect gap semiconductors, [cf. e.g. G. Eda and S. A. Maier, *ACS nano* 7(7), 5660 (2013)].

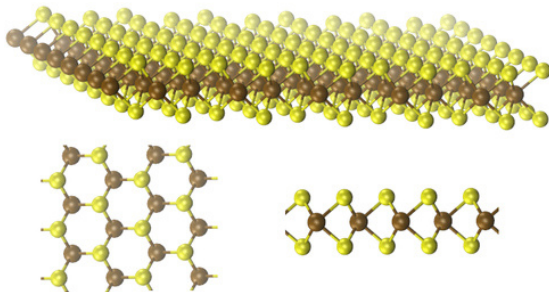


Fig. 2.84: Schematic representation of the structure of a single layer of  $\text{MoS}_2$  shown from different angles, with molybdenum atoms in brown and sulfur atoms in yellow, [<https://www.nano-tcad.ethz.ch/en/more-information/research/ultimate-device-scaling/single-layer-mos2-transistors.html>]

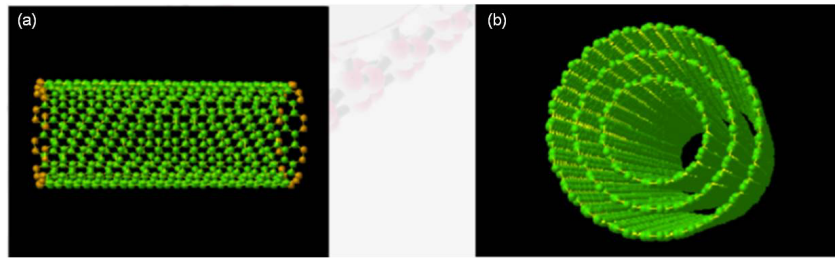


Fig. 2.85: (a) Single-walled CNT: a single atomic layer forms the wall, tube diameter  $\varnothing \sim 0.6\text{-}5\text{ nm}$ ; (b) multi-walled CNT:  $\varnothing_{\text{inner}} \sim 1.5\text{-}15\text{ nm}$ ,  $\varnothing_{\text{outer}} \sim 2.5\text{-}50\text{ nm}$ , up to 50 layers [http://www.eng.uwo.ca/people/jherrera/presentation1.pdf]

## 2.6.2 Carbon nanotubes (CNTs)

Carbon nanotubes can be described as rolled-up graphene ribbons. The cylindrical tubes are typically closed by a hemispherical cap. One can discriminate between **single-walled** and **multi-walled carbon nanotubes**. Single-walled CNTs consist in a single cylinder, while multi-walled CNTs consist in several concentrically stacked cylinders of increasing diameter (see Fig. 2.85). CNTs were first experimentally reported in 1991 by Sumio Iijima et al.. While they abundantly occur naturally e.g. in soot, very high-resolution imaging techniques were required to image single nanotubes, which have diameters on the order of 1 nm. Such techniques were only sufficiently developed by the end of the 20<sup>th</sup> century.

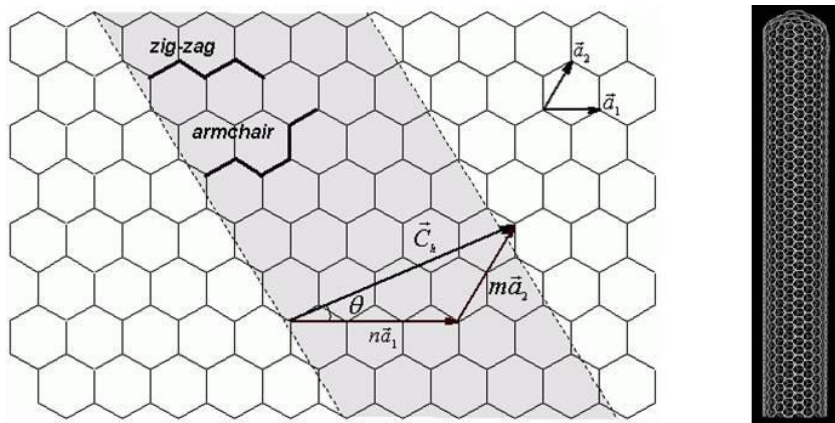


Fig. 2.86: Cut through a graphene sheet to define a nano-ribbon that will be rolled up as a CNT. The vector  $\vec{C}_k$  determines the chiral angle  $\Theta$  and the circumference of the CNT.  $\Theta = 0^\circ$  leads to zig-zag CNTs,  $\Theta = 30^\circ$  to armchair CNTs.

Depending on the angle under which the ribbons are rolled up, three different types of single-walled CNTs are distinguished: **zig-zag**, **armchair**, or **chiral** CNTs. The CNTs are described by the **chiral indices**  $(n, m)$ . Figure 2.86 illustrates the relevant parameters. Each carbon atom in a graphene sheet can be addressed by a vector  $\vec{C}_k = n\vec{a}_1 + m\vec{a}_2$ , where  $\vec{a}_1$  and  $\vec{a}_2$  denote the two vectors inscribing an equilateral triangle into a single honeycomb cell. The vector  $\vec{C}_k$  denotes two points that are connected to form a cylindrical nanotube, thus the vector line will form the circumference of the

CNT. Depending on the way the vector cuts the graphene grid, different circumference lines are observed. When neglecting the handedness of the CNT, the chiral indices can be limited to  $n \geq m \geq 0$ .

For  $(n, m) = (n, n)$  the CNTs are of the armchair type.

For  $(n, m) = (n, 0)$  the CNTs are of the zig-zag type.

For  $(n, m)$  with  $m \notin \{0, n\}$  the CNTs are of the chiral type.

Illustrations of the three types and the corresponding edges are shown in Fig. 2.87.

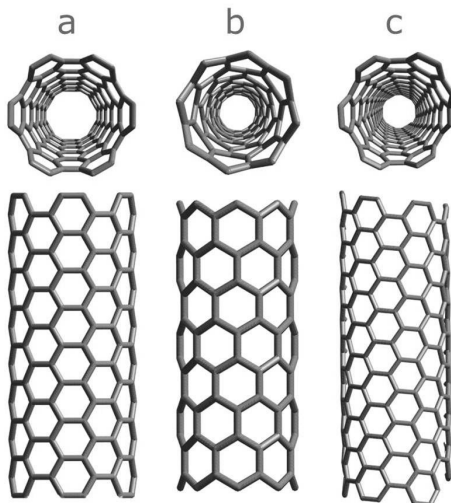


Fig. 2.87: Schematic structure and edge shape of (a) armchair, (b) zig-zag, and (c) chiral CNT [https://sites.google.com/site/cntcomposites/structure-of-cnts]

The distance between two carbon atoms (length of one bond) is  $a_{C-C} = a_0 = 1.42 \text{ \AA}$  (or slightly bigger for very small CNTs due to stretching under high curvature). Accordingly, the length of the vectors  $\vec{a}_1$  and  $\vec{a}_2$  amounts to  $a = 2.46 \text{ \AA}$ .

The diameter  $d$  of the CNTs can be calculated to

$$d = \frac{a}{\pi} \sqrt{n^2 + m^2 + mn} \simeq 0.0783 \text{ nm} \sqrt{n^2 + m^2 + mn} \quad (2.90)$$

The **chiral angle**  $\Theta$  between the vectors  $\vec{a}_1$  and  $\vec{C}_k$  amounts to

$$\tan \Theta = \frac{\sqrt{3}m}{2n+m} \quad (2.91)$$

with  $0^\circ \leq \Theta \leq 30^\circ$  for the above definition of  $(n, m)$ . Simple geometry shows that  $\Theta = 0^\circ$  for zig-zag CNTs,  $\Theta = 30^\circ$  for armchair CNTs, and  $0^\circ < \Theta < 30^\circ$  for chiral CNTs.

Additionally, the chiral index indicates whether the CNTs are metallic or semiconducting. All CNTs with chiral indices for which  $\frac{n-m}{3} \in \mathbb{N}_0$  are metallic, which includes all armchair CNTs. All CNTs with indices for which  $\frac{n-m}{3} \notin \mathbb{N}_0$  are semiconducting.

As a result of these rules, one finds that  $2/3$  of all possible indices lead to semiconducting CNTs, and  $1/3$  to metallic CNTs. Therefore about  $2/3$  of single-walled CNTs are semiconducting and  $1/3$  is metallic. For multi-walled CNTs the possibility to find

metallic CNTs strongly increases due to the increased chances that at least one of the individual cylinders is metallic, allowing for conduction through the CNT.

For the one-dimensional CNTs, the  $k$ -vector becomes quantized, modifying the energy landscape known from graphene. For the energy  $E(\vec{k})$  and the CNT chiral vector  $\vec{C}_k = n\vec{a}_1 + m\vec{a}_2$ , the following quantization condition holds:

$$\vec{k} \cdot \vec{C}_k = 2\pi n \quad \text{with } n = 1, 2, 3, 4, \dots \quad (2.92)$$

The quantization is visualized in Fig. 2.88.

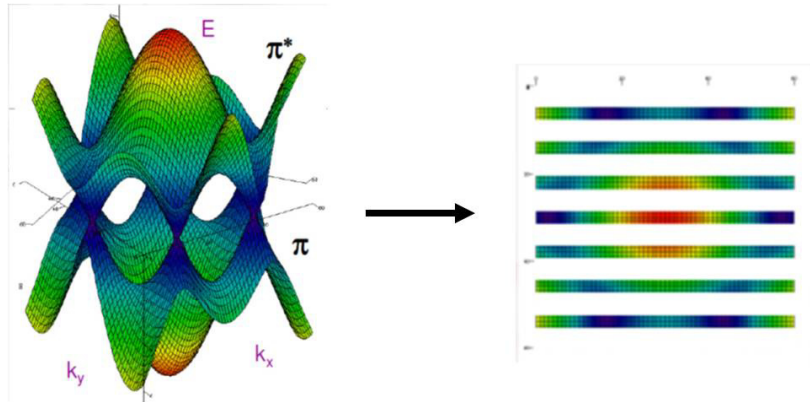


Fig. 2.88: Quantization of the  $k$ -vector for single-walled carbon nanotubes [http://www.eng.uwo.ca/people/jherrera/presentation1.pdf]

As a result, sharp peaks are present in the density of states (DOS) of single-walled CNTs, called **van Hove singularities**. The positions of the peaks depend on the specific chiral indices  $(n, m)$ . While metallic CNTs exhibit a wide spacing between individual singularities with a finite DOS between, the DOS of semiconducting CNTs displays a series of peaks and gap energies with a bandgap around  $E = 0$ , offering possible transitions between states. Examples of the two cases are shown in Fig. 2.89.

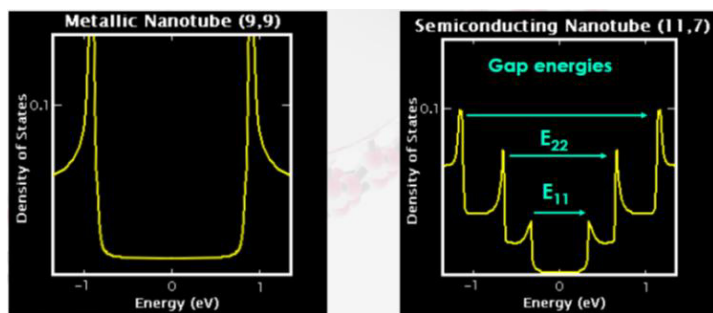


Fig. 2.89: Density of states of (left) metallic and (right) semiconducting single-walled CNTs [http://www.eng.uwo.ca/people/jherrera/presentation1.pdf]

The respective energy separations of the transitions  $E_{ij}$  between states depend critically on the diameter  $d = 0.0783 \text{ nm} \sqrt{n^2 + m^2 + mn}$  of the CNT and are continuously shifted to higher values for smaller CNTs, as calculated in Fig. 2.90. From the equation  $(n - m)/3 \in \mathbb{N}_0$  one can also predict whether the CNT is metallic.

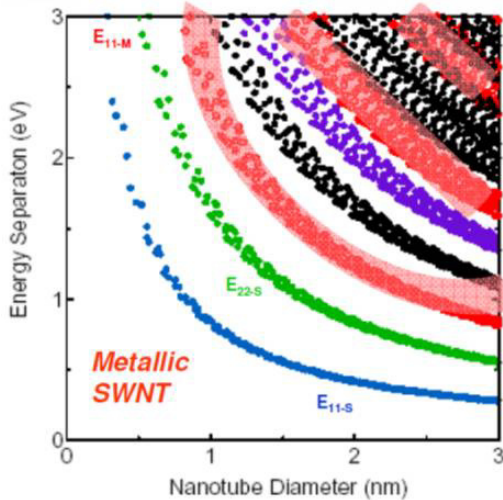


Fig. 2.90: Calculated band gap energies of different transitions within the density of states in dependence of the respective CNT diameter; metallic CNT are marked in red [<http://www.photon.t.u-tokyo.ac.jp/maruyama/kataura/kataura.html>]

Fluorescence measurements can be used to determine the types of chiral indices present in a mix of CNTs. The principle of fluorescence excitation and emission for semiconducting CNTs is schematically outlined in Fig. 2.91(a). Metallic CNTs do not exhibit fluorescence. For the purpose of chiral index distinction the energy of the light for excitation  $E_{ex}$  is varied, and the energy of the emitted light  $E_{em}$  is detected. The measured intensities are plotted as  $I(\lambda_{em}, \lambda_{ex})$ . For certain combinations of  $\lambda_{ex}$  and  $\lambda_{em}$  characteristic intensity maxima appear. Each of these maxima can be assigned to a particular combination of  $(n, m)$ , see Fig. 2.91.

### Preparation of CNTs

The most common preparation techniques for CNTs are

- Chemical vapour deposition (CVD): Substrates with a patterned catalyst are placed in an oven and heated to several 100 °C. A carbon containing gas (e.g. CH<sub>4</sub>, C<sub>2</sub>H<sub>2</sub>) is introduced to the chamber and dissociated at the catalyst. The resulting carbon accumulates on the catalyst and CNTs are grown. Single-walled CNTs can be obtained by preparing nanoscale catalyst dots. The catalyst dot either remains on the substrate (*bottom growth*, e.g. Fe) or at the tip of the CNT (*tip growth*, e.g. Ni).
- Arc discharge: An electric arc occurs in the gas-filled space between two conductive carbon electrodes and results in a very high temperature, such that an evaporation and deposition of carbon particles takes place.
- Laser ablation: A high power laser is used to vaporize carbon from a graphite target at high temperature.

In each case a catalyst is required to initiate single-walled CNT growth (e.g. Fe, Co, Ni). By nanostructuring the catalyst dots, the positions of the CNTs can be exactly

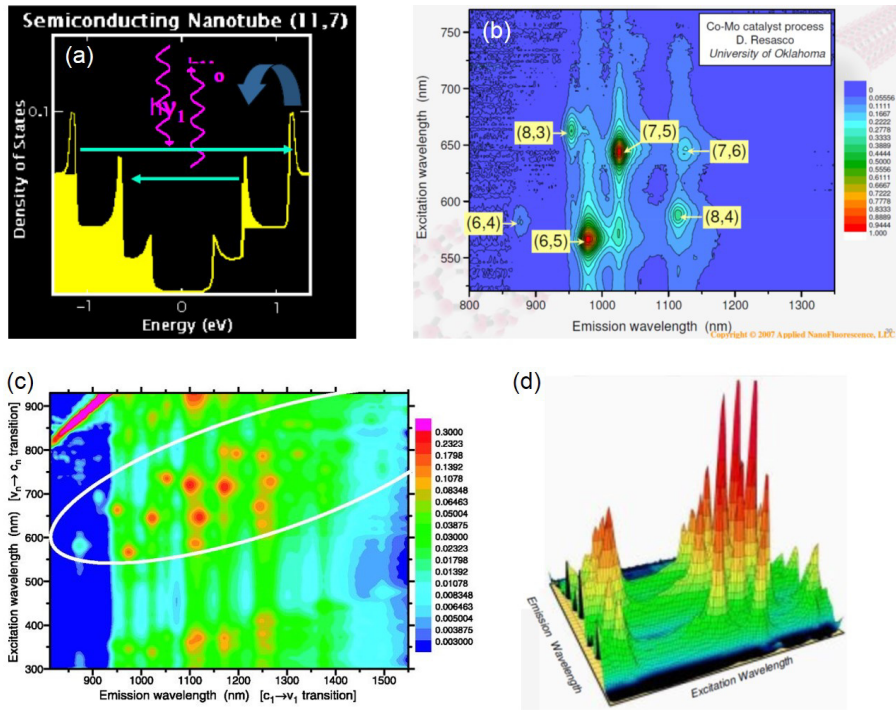


Fig. 2.91: (a) Schematic of fluorescence excitation and emission in CNTs; (b) plot of the excitation versus emission wavelength showing maxima which are assigned to particular  $(n, m)$ ; (c) 2dim and (d) 3dim plot of the excitation vs. emission wavelengths of a mixture of CNTs with different  $(n, m)$  [http://www.eng.uwo.ca/people/jherrera/presentation1.pdf; Applied NanoFluorescence, LLC (2007); Weisman et al., Science 298, 2361 (2002)]

predetermined. The growth direction may be influenced by applying a lateral gas flow or an electric field, using templated substrates, or growing very dense forests. CNTs in solution can be attracted to electrodes by dielectrophoretic forces. An example of vertically grown CNTs is illustrated in Fig. 2.92. By ultracentrifugation, CNT solutions containing almost exclusively CNTs of a single chiral index can be obtained.

## Device applications

CNTs have created interest for different applications due to their excellent mechanical strength, electrical properties, low weight, and nanoscale dimensions. For example CNTs have been implemented as the conducting channel in ultra-small transistors, as field emitters e.g. for TV screens, as highly sensitive gas sensors, and for many material applications, such as carbon fiber enforced sports equipment frames. Some exemplary device schematics are shown in Fig. 2.93. Figure 2.93(a) depicts a multi-walled CNT vertically grown on an electrode. By introducing a counter-electrode in an UHV chamber and applying several 100 V bias, electrons are directionally emitted from the CNT tip, making it a nano-scale electron gun. The emission characteristics of the CNT from (a) are shown in (b). Figure (c) depicts the schematic of a CNT as the conducting channel of a field-effect transistor. CNT transistor channels with channel lengths down to  $< 20$  nm have been demonstrated, beating many Si transistors. A corresponding device with a CNT on the micron-scale connected by source and drain electrodes is shown in (d).

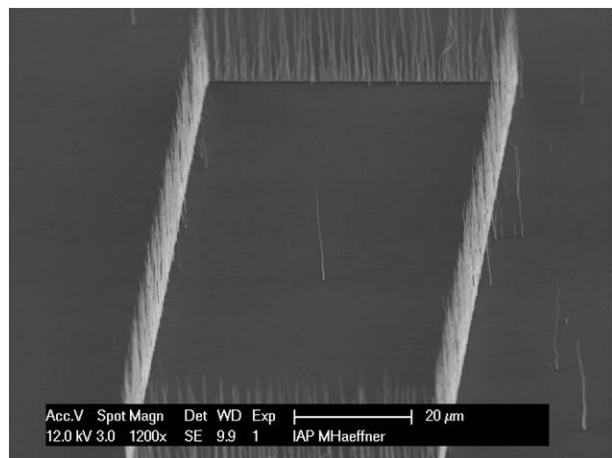


Fig. 2.92: Individually positioned CNTs vertically grown from nanostructured catalyst dots by plasma-enhanced chemical vapour deposition [M. Häffner, AG Kern, University of Tübingen]

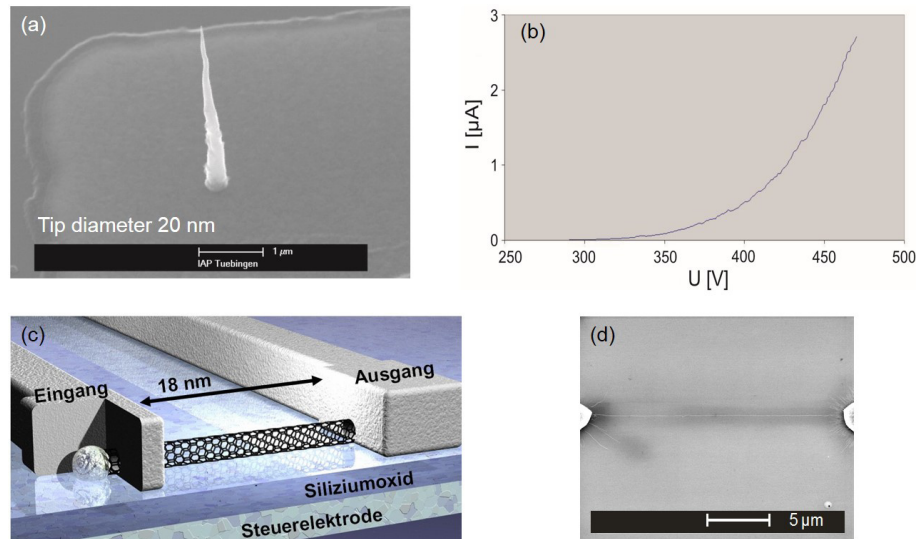


Fig. 2.93: (a) Vertically grown multi-walled CNT on an electrode as a field-emitter; (b) emitter characteristics of the CNT in (a); (c) schematic of a CNT transistor; (d) horizontally grown CNT between two electrodes acting as a transistor channel [R. Löffler, AG Kern, Universität Tübingen; [www.pressebox.de/pressemeldungen/infineon-technologies-ag/](http://www.pressebox.de/pressemeldungen/infineon-technologies-ag/); E. Fischer, AG Kern, Universität Tübingen]

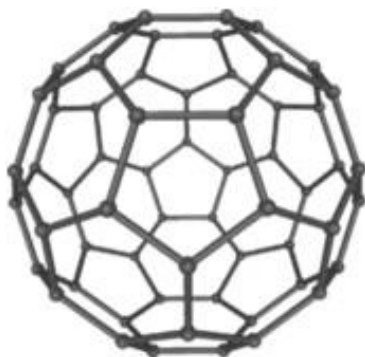


Fig. 2.94: Buckminster fullerene  $C_{60}$  [<http://en.wikipedia.org/wiki/Fullerene>]

### 2.6.3 Buckminster fullerenes

Fullerenes are carbon molecules consisting of  $\sim 20$  to  $200$  carbon atoms with preferred stable, especially spherical, configurations. They were predicted in 1970 by E. Osawa and first observed by H. Kroto, R. Curl and R. Smalley in 1985, who were awarded a shared Nobel prize in 1996. Fullerenes have a natural occurrence e.g. in soot. The historically first reported fullerenes were the Buckminster fullerenes  $C_{60}$  (named after the architect Buckminster Fuller), also called “Bucky balls”, which contain  $60$  carbon atoms ordered in pentagons and hexagons. The soccerball-like structure can be seen in Fig. 2.94. Other fullerene molecules ( $C_n$  clusters) have configurations such as  $C_{20}$ ,  $C_{70}$ ,  $C_{76}$ ,  $C_{82}$ , or  $C_{84}$ . The structures are highly stable without any dangling bonds. The cage structure of the fullerenes can be filled with atoms of different elements, creating so-called **endohedral fullerenes**, which exhibit interesting modified properties. Figure 2.95 shows a single-walled carbon nanotube filled with endohedral fullerenes. Buckminster fullerenes may be prepared by the laser or arc discharge evaporation of graphite. They find applications in electronic devices. As a prominent application they are introduced as acceptors in organic solar cells, in combinations such as DIP: $C_{60}$  or P3HT:PCBM, with PCBM being a modified fullerene molecule. As for graphene, the topological structure of fullerenes has been emulated using other elements, e.g. creating  $B_{60}$  molecules.

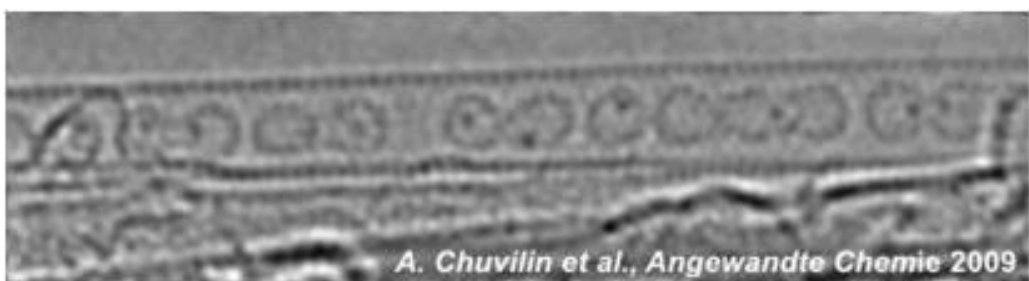


Fig. 2.95: TEM image of a single-walled CNT filled with endohedral fullerenes filled with dysprosium atoms [A. Chuvilin et al., Angewandte Chemie 122(1), 197 (2010)]

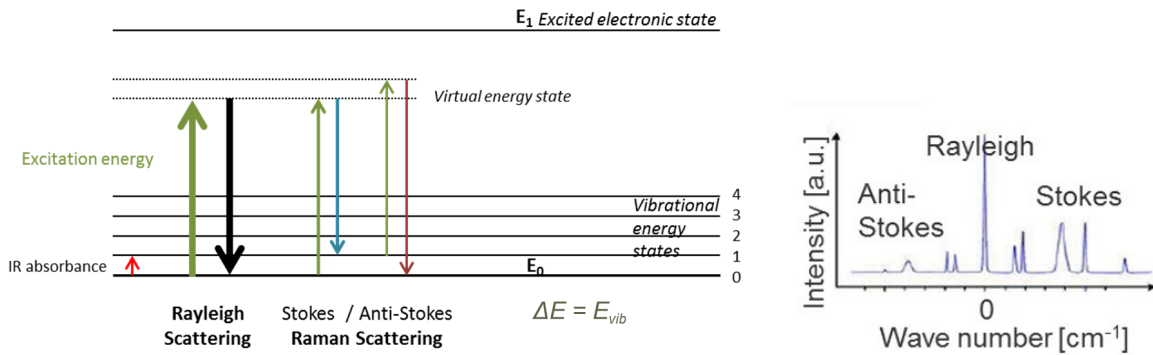


Fig. 2.96: Left: schematic transitions for Rayleigh, Stokes, and anti-Stokes scattering; right: schematic Raman spectrum, with the dominant Rayleigh peak at 0 wavenumbers, and the symmetric peaks of the Stokes and anti-Stokes processes, with a reduced intensity for the anti-Stokes processes [www.wikipedia.de; Witec Webinar 2010]

## 2.6.4 Raman spectroscopy

Raman spectroscopy (named after C.V. Raman) is a powerful technique for gaining chemical and structural information and for material identification. In Raman spectra, the energy loss of light scattered inelastically by a sample upon illumination is recorded. The signal intensity however poses a challenge. Typically over 99% of the light are not scattered, while about 0.1% is elastically scattered, the so-called Rayleigh scattering. Only about  $10^{-4}\%$  to  $10^{-7}\%$  of the light are inelastically scattered, with extremely small scattering cross-sections of molecules of typically  $\sim 10^{-30}$  to  $10^{-25} \text{ cm}^2$ . Under laser excitation and relaxation, molecular vibrations can be excited in the material, which leads to a characteristic energy difference between the incident and re-emitted light. Different types of chemical bonds and of relative motions may be discerned by the characteristic energy loss, which is why the Raman spectrum is often called a “chemical fingerprint”. The energy loss by excitation of vibrations and energy transfer from the photon to the molecule is called the Stokes shift. Analogously, systems that are already in an excited vibrational ground state may transfer energy from the molecule to the photon upon illumination. In this case the energy of the light re-emitted to the ground state is increased by the same energy difference between the ground and the excited state in the incident light. The anti-Stokes spectrum is thus symmetric in wavenumbers to the Stokes spectrum. However anti-Stokes processes occur with lower intensity, since the probability of the process is much lower than for the Stokes process. A schematic energy scheme of the Rayleigh, Stokes and anti-Stokes Raman processes as well as a model Raman spectrum are shown in Fig. 2.96.

On the  $x$ -axis of Raman spectra the Raman shift is given in the unit of **wavenumbers** ( $\tilde{\nu} = 1/\lambda$ , given in  $\text{cm}^{-1}$ ). The wavenumber corresponds to the difference of the inverses of the excitation and the emission wavelengths, or to the energy difference between the excitation and emission normalized by  $hc$ :

$$\text{Raman shift} = \Delta\tilde{\nu} = \frac{1}{\lambda_0} - \frac{1}{\lambda_1} = \frac{E_0 - E_1}{hc} \quad (2.93)$$

The Raman shift, i.e. the energy loss or gain detected in the Raman spectra of

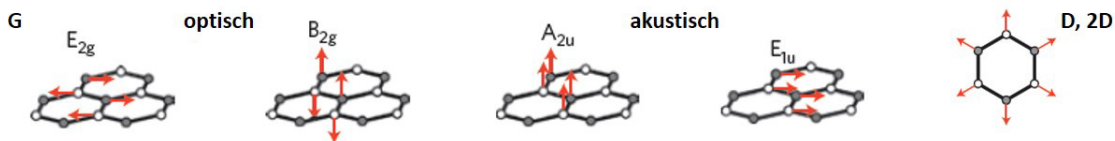


Fig. 2.97: Different molecular vibrations of the carbon atoms in a graphene lattice, leading to characteristic Raman peaks (e.g. G, D, 2D peak) [A.C. Ferrari et al., *Nature Nanotechnol.* 8, 235 (2013), M. Hall, Thermo Fisher Scientific Webinar (2013)]

graphene, corresponds to relative motions of the carbon atoms within the lattice, which are connected with characteristic phonon energies. Some such vibrational modes are depicted in Fig. 2.97. In order for modes to be Raman active, a change in the polarizability of the molecule  $\alpha$  has to occur during the vibration. Out-of-plane phonon modes are not Raman active, and cannot be detected in Raman spectra. They could however be discerned by infrared spectroscopy, for which the molecule instead has to undergo a change of the dipole moment during the vibration. The optical in-plane Raman mode results in the characteristic **G-peak**, while the radial breathing mode, a radial oscillation of the carbon ring, is responsible for the **D-peak** (also “defect peak”), as well as for the **2D-peak** at twice the wavenumber of the D-peak.

The D, G and 2D peaks occur at roughly the same spectral positions for all carbon materials. Their absolute and relative intensities, full-widths-at-half-maximum, minute shifts, potential peak splittings, and the occurrence of additional peaks however provide a wealth of information on the carbon structure and properties. The ratio between the D and G peaks is indicative of the purity of the material. The number of graphene sheets (single-layer versus double-layer, triple-layer etc. or bulk graphite  $\doteq$  multi-layer graphene) can be discerned from the ratio between the 2D and G peaks. A high  $I_{2D}/I_G$  ratio indicates single layer graphene, as demonstrated in Fig. 2.99.

**G-peak:** The G-peak is a first-order peak and corresponds to an  $sp^2$ -C-C vibration. It occurs at  $\sim 1585\text{ cm}^{-1}$ . Uni-axial stretching leads to a splitting of the G-peak into two peaks. p-doping manifests itself as a blue shift, and n-doping as a red shift, while hydrostatic pressure also leads to a frequency shift.

**D-peak:** The D- (or “defect”) peak stems from radial breathing modes of the hexagonal carbon rings and occurs at  $\sim 1250 - 1400\text{ cm}^{-1}$ . A high intensity D-peak is the most dominant sign of defects or disorder. Both the intensity and full-width-at-half-maximum give information about defects. The line width may vary from  $\sim 7$  to several hundred  $\text{cm}^{-1}$ .

**2D-peak:** The 2D-peak is a 2<sup>nd</sup> order process involving two-phonon processes. It occurs at twice the wavenumber of the D-peak, i.e. at  $\sim 2500 - 2800\text{ cm}^{-1}$ . This peak is an important indicator for the identification of the number of graphene sheets and the layer stacking. It can thus be used for single-layer graphene identification, as shown in Fig. 2.98.

For perfect single-layer graphene, the intensity ratio  $I_{2D}/I_G$  can be up to 24. For increasing layer numbers the intensity ratio decreases significantly. For multi-layer graphene, splitting of the 2D-peak into several peaks may be observed.

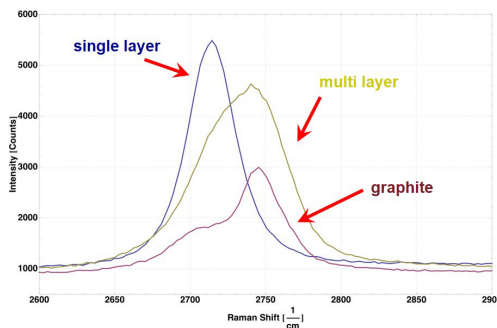


Fig. 2.98: Decreasing intensity and increasing peak splitting of the 2D-peak for an increasing number of graphene layers [A. Jorio, ISRN Nanotechnology 2012, 1 (2012)]

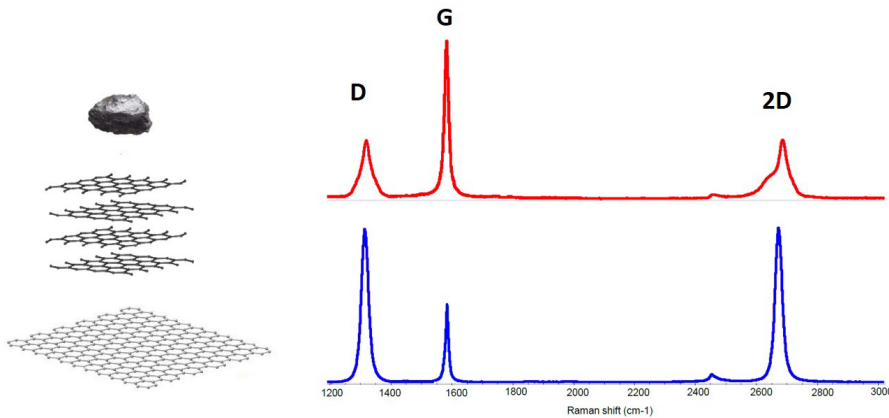


Fig. 2.99: Sample Raman spectra of graphite (top) and graphene (bottom), where a high  $I_{2D}/I_G$  ratio is seen for the single-layer graphene [A.C. Ferrari et al., Nature Nanotechnol. 8, 235 (2013), M. Hall, Thermo Fisher Scientific Webinar (2013)]

Additional peaks may occur, which are mostly linked to impurities and defects, since defect scattering is required for their activation. An increased number of additional peaks ( $D'$ ,  $D+D''$ ,  $D+D'$ ,  $2D'$ , ...) points towards high-defect, lower quality graphene. An example of low defect versus high defect graphene layers is shown in Fig. 2.100.

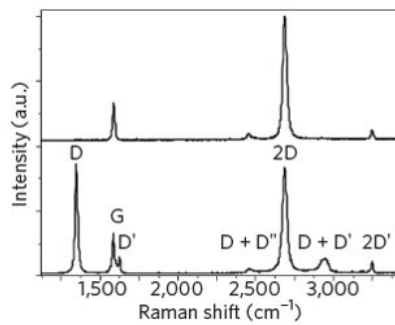


Fig. 2.100: Raman spectrum of high quality, low defect graphene (top) versus high defect graphene (bottom) [A.C. Ferrari et al., Nature Nanotechnol. 8, 235 (2013)]

Apart from the number of graphene layers and the defects in a carbon system, information about further parameters can be gained from Raman spectra: Carbon configuration (single/double bonds), stress/strain, doping, crystal structure, temperature, ... Raman spectroscopy thus offers a powerful tool for (nano-)carbon characterization.

### Raman spectra of carbon nanotubes

Moving from Raman spectra of graphene to Raman spectra of single-walled carbon nanotubes, another parameter can be extracted. Carbon nanotubes exhibit **radial breathing modes** as well, only in this case the whole nanotube radially expands and contracts in the vibration, as schematically shown in Fig. 2.101. These radial breathing modes can be detected in the low wavenumber range of the Raman spectrum, at few  $100\text{ cm}^{-1}$ , and are characteristic for each specific carbon nanotube. If a nanotube with chiral indices  $(n, m)$  is modeled as a homogeneous cylinder, the frequency of the radial oscillations is proportional to the inverse diameter  $1/d$ :

$$\Delta\tilde{\nu}_{RBM} = \frac{c_1}{d} + c_2 \quad (2.94)$$

where  $c_1$  and  $c_2$  are constant experimentally determined fit parameters, and the diameter of the nanotube  $d$  is given as

$$d = \frac{a}{\pi} \sqrt{n^2 + m^2 + mn} \quad (2.95)$$

with  $a = 2.46\text{ \AA}$  the in-plane lattice constant of graphene. Thus direct conclusions on the nanotube geometry and chirality can be drawn from the Raman spectrum.

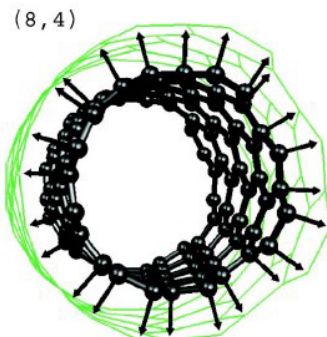


Fig. 2.101: Schematic of a (8,4) carbon nanotube expanding in radial breathing modes